Introducing a Dynamic Reconstruction Methodology for Multilayered Structures in Atom Probe Tomography

Constantinos Hatzoglou, Gérald da Costa, Peter Wells, Xiaochen Ren, Brian Geiser, David Larson, Rémi Demoulin, Kasper Hunnestad, Etienne Talbot, Baishakhi Mazumder, et al.

https://doi.org/10.1093/micmic/ozad054

Introducing a Dynamic Reconstruction Methodology for Multilayered Structures in Atom Probe Tomography

Constantinos Hatzoglou[1,2,*] Gérald Da Costa[1], Peter Wells[3], Xiaochen Ren[3] , Brian P. Geiser[4], David J. Larson[4] , Remi Demoulin[1], Kasper Hunnestad[2] , Etienne Talbot[1], Baishakhi Mazumder[5], Dennis Meier[2], and François Vurpillot[1]

[1]*INSA Rouen Normandie, CNRS, Groupe de Physique des Matériaux UMR 6634, Univ Rouen Normandie, INSA Rouen Normandie, CNRS, Groupe de Physique des Matériaux UMR 6634, Rouen F-76000, France*
[2]*Department of Materials Science and Engineering, NTNU, Norwegian University of Science and Technology, Trondheim 7491, Norway*
[3]*Intel Corporation, Hillsboro, OR 97124, USA*
[4]*CAMECA Instruments Inc., 5470 Nobel Dr., Madison, WI 53711, USA*
[5]*Department of Material Design and Innovation, University at Buffalo, Buffalo, NY 14260, USA*

***Corresponding author:** Constantinos Hatzoglou, E-mail: constantinos.hatzoglou@ntnu.no

Abstract

Atom probe tomography (APT) is a powerful three-dimensional nanoanalyzing microscopy technique considered key in modern materials science. However, progress in the spatial reconstruction of APT data has been rather limited since the first implementation of the protocol proposed by Bas et al. in 1995. This paper proposes a simple semianalytical approach to reconstruct multilayered structures, i.e., two or more different compounds stacked perpendicular to the analysis direction. Using a field evaporation model, the general dynamic evolution of parameters involved in the reconstruction of this type of structure is estimated. Some experimental reconstructions of different structures through the implementation of this method that dynamically accommodates variations in the tomographic reconstruction parameters are presented. It is shown both experimentally and theoretically that the depth accuracy of reconstructed APT images is improved using this method. The method requires few parameters in order to be easily usable and substantially improves atom probe tomographic reconstructions of multilayered structures.

Key words: atom probe tomography, dynamic reconstruction, field evaporation simulation, multilayered structure

Introduction

Atom probe tomography (APT) provides the three-dimensional (3D) reconstruction of elemental maps within a small probed volume of material with near-atomic resolution (Miller, 2000; Gault et al., 2012; Larson et al., 2013; Lefebvre et al., 2016). In APT, atoms are progressively evaporated from the surface of a needle-shaped specimen under the effect of an intense electric field. The electric field is generated by the application of a high voltage onto a specimen prepared as a sharp needle. The apex of the needle can be approximated by a nearly hemispherical apex with a radius of curvature ranging from 30 to 200 nm. Analyses are generally performed at cryogenic temperatures (20–100 K). The diverging electric field existing near this apex accelerates the ionized atoms away from the specimen surface. Ions are collected by a position-sensitive detector.

Using a relatively simple reverse-projection algorithm, combined with an incremental increase in the depth, the impact coordinates of each ion on the detector are used to build a tomographic reconstruction of the field-evaporated volume within the field of view of the microscope (Bas et al., 1995; Geiser et al., 2009; Gault et al., 2011*a*, 2011*b*). It can be determined either by correlative microscopy of APT and transmission electron microscopy (TEM) (Haley et al., 2011; Herbig et al., 2015) or by field evaporation simulation (Beinke et al., 2016). Up to now, the most common approach is to use an analytical approach where the impact coordinates on the detector and the detection event sequence are considered. This then requires reconstruction parameters to be defined. However, in this case, it has been demonstrated experimentally (Gault et al., 2011*a*, 2011*b*) and numerically (Mesa et al., 1996; Vurpillot et al., 2011) that it is generally a severe simplification to consider the reconstruction parameters as constant. The reconstruction parameters, used to calculate magnification from the beginning to the end of the analysis, can vary by several tens of percent over the volume, which is detrimental to the reconstruction accuracy. This evolution strongly depends on the sample morphology. Instead, the parameters need to be adjusted throughout the reconstruction (Larson et al., 2011), then called dynamic reconstruction (DR).

As demonstrated by Hatzoglou et al. (2019), for a single-phase material, the evolution of the reconstruction parameters [field factor and image compression factor (ICF)] can be estimated using field evaporation simulation. In this study, we expand this approach toward multilayered systems composed of two or more materials. The evolution of the parameters is then injected into the reconstruction protocol, using the GPM 3D APT data treatment software. Additionally, the Norwegian Atom Probe App (NAPA) software has been used. It was developed by Hatzoglou (2022) from the Norwegian University of Science and Technology (NTNU) and is an open-access software program dedicated to APT data treatment.

After a brief presentation of the reconstruction parameters, field evaporation simulation results of multilayered structures will be presented, as well as the evolution of the reconstruction parameters. Regarding simulation results, an analytical expression of this evolution, composed of few parameters, will be proposed. This DR will be applied to different multilayered structures: $In_{0.15}Al_{0.85}N$/GaN, Si/SiGe, Si/SiO_2, and $LuFeO_3$. The improvement and performance of the DR will be discussed, and it will be presented in each case how to estimate the additional reconstruction parameters induced by the dynamic approach, without performing electron tomography (Fletcher et al., 2022).

Dynamic Reconstruction

Reconstruction Parameters

Once ionized and desorbed from the surface, ions are accelerated by the surrounding electric field toward the detector. As the ion trajectories in the vicinity of a real sample are very complex (Vurpillot et al., 1999; Vurpillot & Oberdorfer, 2015), extensive works have been done to simplify the problem and to define a simple projection law describing the imaging process. The simplest model assumes that ions follow straight trajectories, and this approach is often used to describe the ion projection in APT and perform a 3D reconstruction. This reconstruction is made *a posteriori*, using data that are available from the analysis of the specimen (e.g., crystallographic feature, particles with known morphology, etc.). The reconstruction is built atom-by-atom by reverse-projecting the detected position onto the surface of a virtual specimen. Details can be found in Miller & Forbes (2009), Gault et al. (2012), Larson et al. (2013), Vurpillot et al. (2013*a*, 2013*b*), and Lefebvre et al. (2016). The lateral coordinates of the ions are deduced from a direct reverse-projection of the ion impact coordinates on the position-sensitive detector back onto a virtual spherical cap, which represents the specimen. The reconstruction in the depth direction is based on a sequential displacement of a virtual ion-emitting surface. Both are based on the estimation of the magnification (M):

$$M \approx \frac{L}{\xi R}, \tag{1}$$

with L the flight path, R the radius of curvature of the specimen, and ξ the ICF. This last factor reflects the compression of the field lines due to the nonsymmetrical nature of the electrostatic environment. The core of the reconstruction process requires accurate knowledge of the radius of curvature (R) for each ion detected to compute its original location at the specimen surface. Different methods have been proposed to estimate R. The first method, named cone angle calculation (Jeske & Schmitz, 2001; Larson et al., 2013), assumes a simplified geometry of the specimen, with an initial radius of curvature (R_0) and a defined shank angle (γ) (Walck et al., 1986). Then, the evolution of the radius of curvature, as a function of the depth (z), is estimated according to the following relationship, which is derived from simple geometric considerations:

$$R = R_0 + \frac{\sin(\gamma)}{1-\sin(\gamma)} z. \tag{2}$$

Considering that the electric field at the specimen surface is close to the evaporation field of the probed material (F_{ev}), then the radius of curvature can also be directly estimated from the applied voltage (V) at the time that the ion is detected:

$$R = \frac{V}{k_f F_{ev}}, \tag{3}$$

with k_f the field factor. This second approach will be referred to as the standard reconstruction protocol.

Determination of several parameters is therefore necessary. The field factor (k_f) and the ICF (ξ) are commonly set as constant parameters. However, it has been demonstrated experimentally (Gault et al., 2011*a*, 2011*b*) and numerically (Mesa et al., 1996; Larson et al., 2011; Vurpillot et al., 2011) that it is generally a strong simplification. Indeed, the field factor and the ICF evolve as a function of the sample morphology and must be adjusted throughout the reconstruction algorithm: $k_{f,i}$ and ξ_i with the ith considered evaporated ions. Hatzoglou et al. (2019) determined analytic expressions that describe the evolution of those parameters ($k_{f,i}$ and ξ_i) during evaporation, for a single-phase material (phase α), based on field evaporation simulation results (Fig. 1a):

$$k_{f,i} = k_{f,0} \times \left(\frac{\exp(\Omega)}{\exp\left(W\left(\frac{V_0}{V_i}\right)\right) - \ln\left(\frac{V_0}{V_i}\right)} \right), \tag{4}$$

$$\xi_i = \xi_0 \times \sqrt[3]{\frac{k_{f,i}}{k_{f,0}}}, \tag{5}$$

with Ω a constant defined as the unique real number that satisfied the equation $\Omega\exp(\Omega) = 1$ (this constant is approximatively equal to 0.567) and W the Lambert function [with $W(1) = \Omega$]. V_i and V_0 are the voltage for the ith ion and the voltage at the beginning of the sample evaporation, respectively. It is the total voltage (i.e., specimen voltage plus pulse voltage). In the same manner, $k_{f,0}$ and ξ_0 are, respectively, the field factor and the ICF at the beginning of the evaporation. Equation (4) represents a development of that presented in Hatzoglou et al. (2019), which has the advantage that it is no longer dependent on the shank angle (γ).

However, equations (4) and (5) are no longer valid when the microstructure becomes more complex. In fact, adding a second phase (β), as a layer perpendicular to the evaporation direction, the evolution of the reconstruction parameters during evaporation (Figs. 1b, 1c), estimated from field evaporation simulation (Vurpillot et al., 2013*a*, 2013*b*), is more complex than that for a single phase. The evolution is also strongly dependent on the evaporation field ratio of the layer ($F_{ev,\beta}$) and the phase in which the layer is embedded ($F_{ev,\alpha}$). In this case, new expressions must be developed to predict the evolution of the reconstruction parameters for such multilayered structures.

From Homogeneous Materials to Multilayered Systems

As in Hatzoglou et al. (2019), field evaporation simulations (Vurpillot et al., 2013*a*, 2013*b*) are used to estimate the evolution of the reconstruction parameters through the evaporation of a multilayered structure. It must be noted that this simulation model is available in the IVAS software (CAMECA Instruments Inc.). Only the radius of curvature of the sample and its shank angle (R_0 and γ) are inputs for

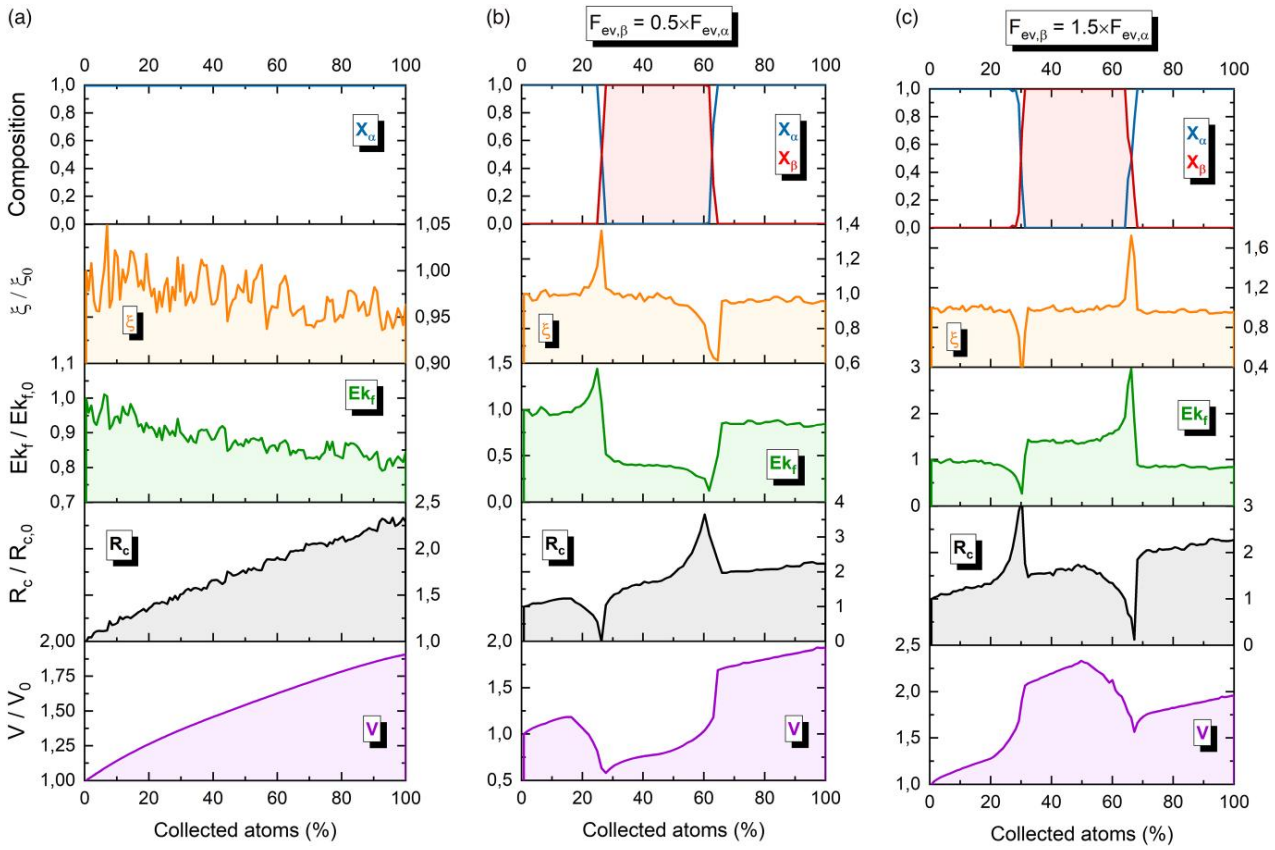

Fig. 1. Evolution of the chemical composition (X_α and X_β) and the evolution of the relative compression factor (ξ), the field factor (Ek_f), the radius of curvature (R_c), and the potential (V) during the evaporation process for different microstructures: (**a**) a single phase (α) and a structure with a layer (β) having (**b**) a higher evaporation field ($F_{ev,\beta} = 1.5 \times F_{ev,\alpha}$) or (**c**) a lower evaporation field ($F_{ev,\beta} = 0.5 \times F_{ev,\alpha}$) than the surrounding α phase (Vurpillot et al., 2013*a*, 2013*b*).

field evaporation simulation of a homogenous or single-phase material, while the layer thickness and evaporation field of the second phase are added here for a multilayered structure (e the thickness and $F_{ev,\beta}$). Field evaporation simulations of several hundreds of different geometrical cases [R_0 from 20 to 100 simulation unit cells (uc) and γ from 5 to 45°] and layer properties (e from 2 to 200 uc and $F_{ev,\beta}$ from 0.5 to 2 times $F_{ev,\alpha}$) were simulated to explore in detail all the configurations. The observations presented below are a synthesis of these simulations and reflect the obtained results. The simulations presented to illustrate the results are the following: $R_0 = 50$ uc, $\gamma = 10°$, $e = 100$ uc, and $F_{ev,\beta}$ is equal to 0.5 or 1.5 times $F_{ev,\alpha}$.

Considering the standard reconstruction protocol, it is not mandatory to determine separately the field factor and the ICF evolution, since the relevant parameter, the magnification, is proportional to their ratio:

$$M_i = \frac{LE_i k_{f,i}}{\xi_i V_i}, \tag{6}$$

with E_i the electric field (considered close to the evaporation field). This ratio can then be developed as a product of two terms:

$$\frac{E_i k_{f,i}}{\xi_i} = \mu_i \times \frac{E_i^* k_{f,i}^*}{\xi_i^*}, \tag{7}$$

with

$$\mu_i = \frac{E_i k_{f,i}}{E_i^* k_{f,i}^*} \times \frac{\xi_i^*}{\xi_i}. \tag{8}$$

The term $(\boldsymbol{E_i^* k_{f,i}^* / \xi_i^*})$ describes the evolution of the reconstruction parameters for a reference phase (i.e., this reference phase is a single-phase material of the same morphology analyzed with the same instrumental parameters). In this case, only the sample morphology determines the evolution of the magnification, and this evolution is integrated into this term. The second term ($\boldsymbol{\mu_i}$) describes the influence of the analyzed multilayered structure on the overall evolution of the magnification during the analysis. All the terms indexed by a star refer to this reference phase. In the case studied here (Figs. 1b, 1c), the reference phase is the phase $\boldsymbol{\alpha}$, and in a more general case, the first evaporated phase will always be taken as the reference one. Combining equations (6) and (8), it clearly appears that the term ($\boldsymbol{\mu_i}$) reflects the magnification fluctuations induced by the microstructure relative to a single-phase material (hence the choice of this letter for this variable):

$$\mu_i = \frac{M_i}{M_i^*} \times \frac{V_i}{V_i^*}, \tag{9}$$

with V_i^* the evolution of the potential if the sample was a single phase. If the analyzed sample corresponds to a single-phase

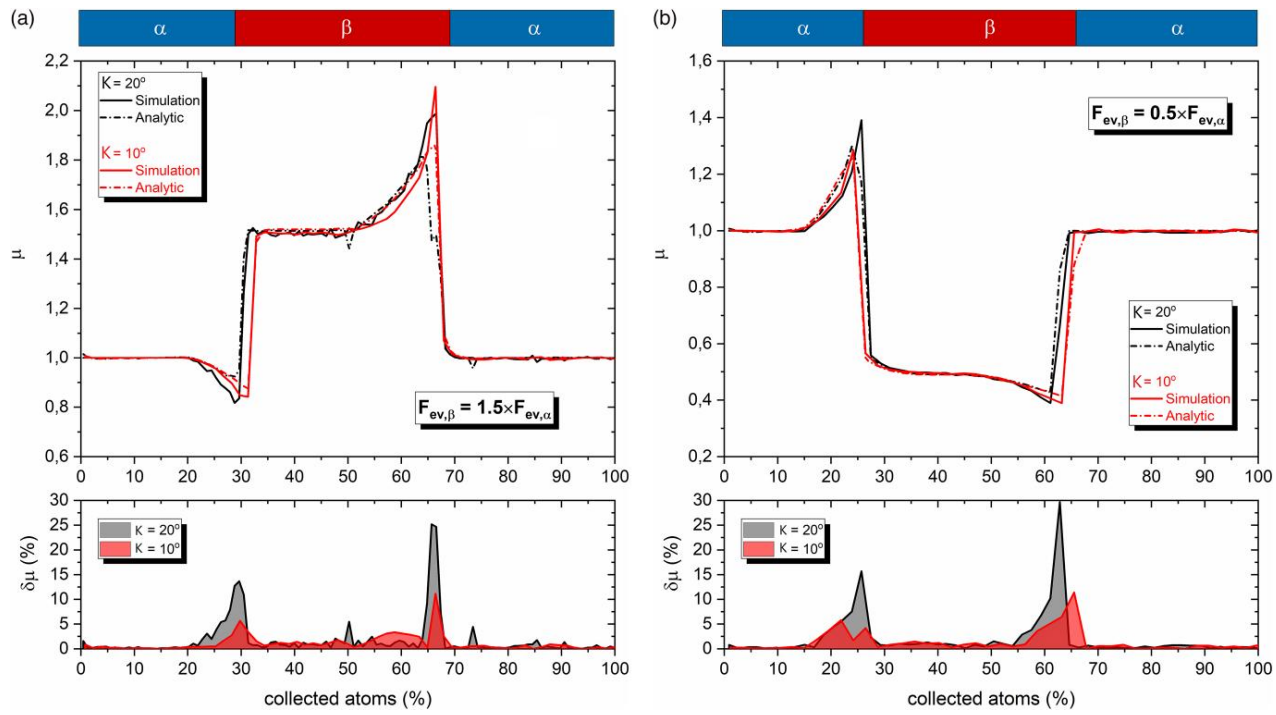

Fig. 2. Evolution of the parameter μ during the evaporation process for a structure with a phase β having (**a**) a higher evaporation field ($F_{ev,\beta} = 1.5 \times F_{ev,\alpha}$) or (**b**) a lower evaporation field ($F_{ev,\beta} = 0.5 \times F_{ev,\alpha}$) than the neighboring phase α. The evolution is estimated from field evaporation simulation results (reported as simulation) using the analytical equation (10), for two different collection angles (K): 10 and 20°. The evolution of the relative error $\delta\mu_i$ (%) is also reported for both cases.

material, in this case, μ_i is equal to 1 [equations (8) and (9) since $V_i = V_i^*$], verifying then that the evolution of the reconstruction parameters matches well with a single phase [equation (7)]. Since the term $(E_i^* k_{f,i}^* / \xi_i^*)$ refers to a single phase, its evolution is already known based on equations (4) and (5). Thus, it remains only to estimate the evolution of μ_i, using field evaporation simulation results (Figs. 2a, 2b). Its estimation is done each time with two simulations, with and without a second layer, and both with the same radius of curvature and shank angle. First, μ_i [equation (8)] can be simplified to the following equation (10), considering equation (5), but also the following obvious equalities: $k_{f,0} = k_{f,0}^*$ and $\xi_0 = \xi_0^*$.

$$\mu_i = \frac{E_i}{E_i^*} \times \left(\frac{k_{f,i}}{k_{f,i}^*} \right)^{\frac{2}{3}}. \tag{10}$$

Second, whatever the simulated layer thickness (e) and evaporation field ($F_{ev,\beta}$) are, the ratio $k_{f,i}/k_{f,i}^*$ can be approximated by the following empirical analytical expression:

$$\frac{k_{f,i}}{k_{f,i}^*} = \frac{E_i}{E_i^*} \times \frac{V_i^*}{V_i}. \tag{11}$$

This last expression suggests that the evolution of the radius of curvature ratio R_i^*/R_i is equal to $(k_{f,i}/k_{f,i}^*)^2$ [considering equation (3)], which was verified from the simulation data. Since the electric field is considered to be close to the evaporation field, E_i^* is equal to $F_{ev,\alpha}$ and E_i can be approximated by an average evaporation field $X_{\alpha,i}F_{ev,\alpha} + X_{\beta,i}F_{ev,\beta}$, with $X_{\alpha,i}$ and $X_{\beta,i}$, respectively, the abundancy of atoms from phases α and β, in the detector referential, subsequently reported as phase concentration. The expression of the evolution μ_i finally becomes:

$$\mu_i = \left(X_{\alpha,i} + X_{\beta,i} \left(\frac{F_{ev,\beta}}{F_{ev,\alpha}} \right) \right)^{\frac{5}{3}} \times \left(\frac{V_i^*}{V_i} \right)^{\frac{2}{3}}, \tag{12}$$

which reproduces the simulation results (Fig. 2). Let us take as an example layer β, with an evaporation field higher than the phase α (Fig. 2a), to discuss the evolution of μ_i and its analytical expression, based also on the numerous observations of similar microstructures in the literature (Larson et al., 2011, 2012; Marquis et al., 2011; Haley et al., 2013, 2018; Rolland et al., 2015*a*, 2015*b*; Xu et al., 2015; Vurpillot et al., 2016; Rolland et al., 2017). At the beginning of the evaporation, i.e., in the core of phase α, μ_i is equal to 1, since this phase is set as the reference one ($V_i = V_i^*$, $X_{\alpha,i} = 1$, and $X_{\beta,i} = 0$). At the interface α/β, first, there is a drop of μ_i, corresponding to the decrease of the magnification, induced by the increase in the mean radius of curvature (Fig. 1b, flattened interface). Indeed, the evaporation rate of the layer β is lower than the phase α (due to its higher evaporation field). There is therefore a decrease in μ_i since the potential increases, compared with the reference one (Fig. 1a), then $V_i^*/V_i < 1$. Second, still at this interface, there is an important growth of μ_i, as then mostly evaporation of the layer β occurs, ($X_{\beta,i} > X_{a,i}$ in Fig. 1b), with $F_{ev,\beta} > F_{ev,\alpha}$. This continues up to a stabilization of μ_i, corresponding then to a complete evaporation of the phase α ($X_{\alpha,i} = 0$) and to the phase β equilibrium. The stabilized value of μ_i is equal to the evaporation field ratio $F_{ev,\beta}/F_{ev,\alpha}$. The potential ratio V_i/V_i^* is constant and equal to $F_{ev,\beta}/F_{ev,\alpha}$ at this evaporation step (combining results in Fig. 1). During the evaporation of the interface β/α, the reverse

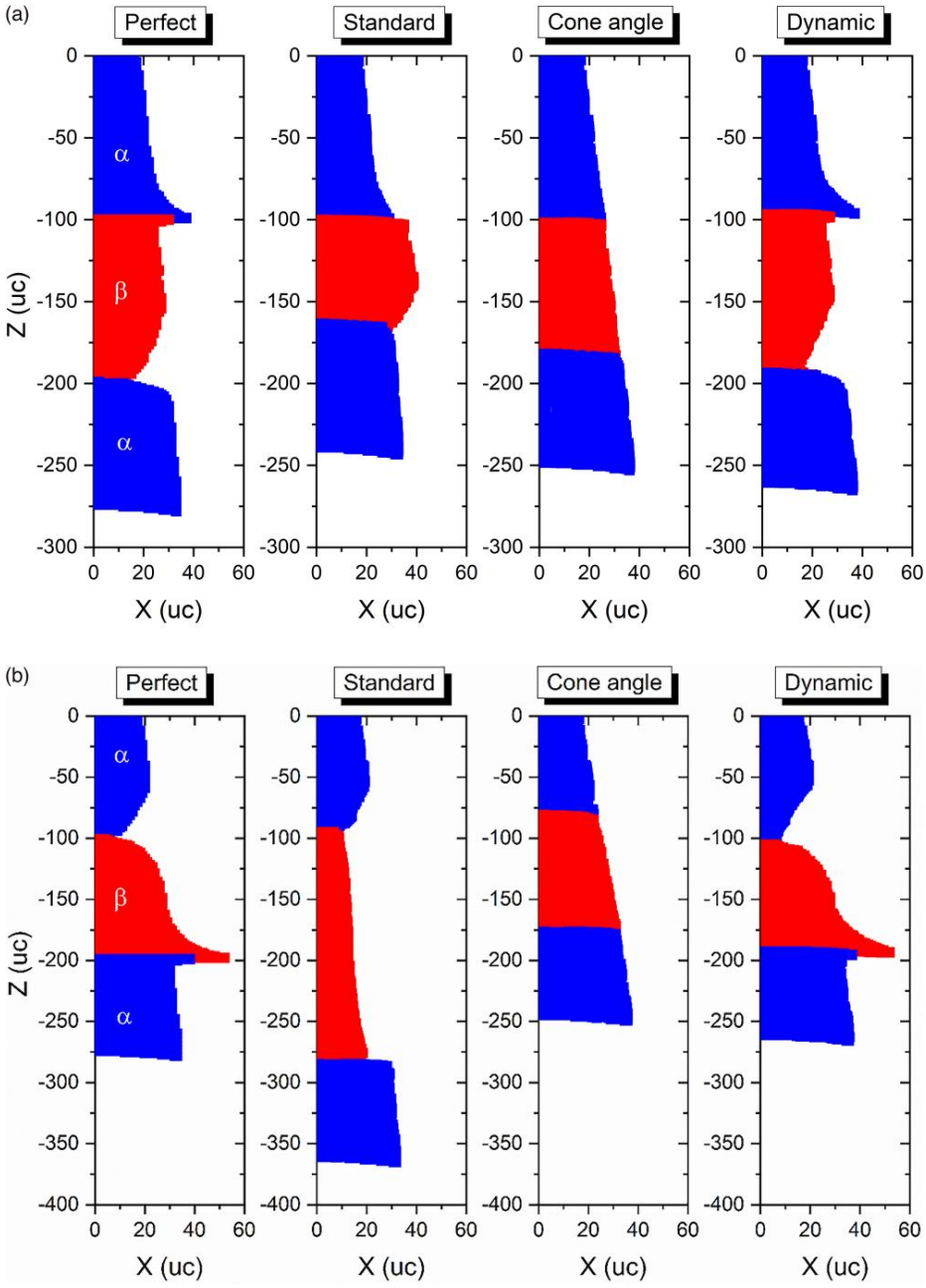

Fig. 3. Reconstruction of a multilayered material with a layer β, sandwiched between two layers α, field evaporated by simulation, using a standard reconstruction protocol, a cone angle protocol, and the dynamic one, compared with the original position (defined as perfect reconstruction), as a function of the evaporation field of the layer: (**a**) $F_{ev,\beta} = 1.5 \times F_{ev,\alpha}$ and (**b**) $F_{ev,\beta} = 0.5 \times F_{ev,\alpha}$. The collection angle is set to 10°. uc is the simulation unit cell.

phenomenon is observed. The phase β is protruding, since its evaporation field is higher than the phase α below, decreasing the mean radius at the apex, thus increasing the magnification (as well as the parameter μ_i). At the end of layer evaporation, there is a drastic drop, corresponding to phase α tending to the equilibrium. Once the evaporation achieves exclusively the phase α, μ_i becomes constant since the reference phase is reached. For the low evaporation field layer (Fig. 2b), it is the same case as the previous one, except that the interface order is reversed.

Overall, the analytical expression of μ_i matches well with the simulation results. It should be noted that this analytical expression also reproduces well all the simulation results that have been carried out by varying the simulation parameters (R_0, γ, e, and $F_{ev,\beta}$). However, there remain some regions, particularly at the interface, where deviations exist (relative error $\delta\mu$ in Fig. 2). By reducing the collection angle (K) from 20 to 10°, this deviation is minimized (Fig. 2). This reduction is not an issue, because it is well known that it generally optimizes the reconstruction of such microstructures (Vurpillot et al., 2004). However, in return, the reconstructed volumes and the number of atoms are reduced, which then increase the measurement uncertainties. In practice, the volume reduction is done on the experimental data by decreasing artificially

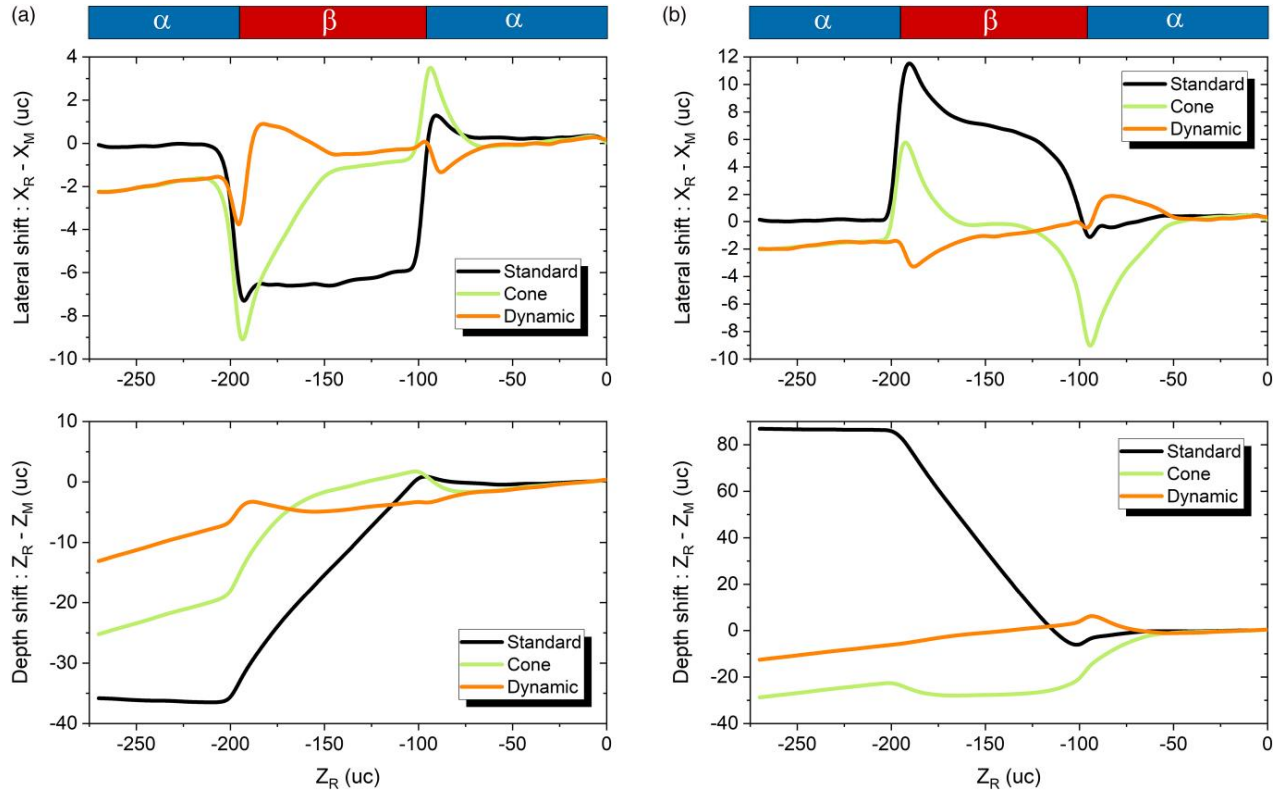

Fig. 4. Lateral (X) and depth (Z) shifts (in uc) between the perfect (X_R and Z_R) and reconstructed positions (X_M and Z_M) as a function of the perfect depth Z_R (uc) for different reconstruction protocols (standard, cone, and dynamic) and different evaporation fields of the layer: (**a**) $F_{ev,\beta} = 1.5 \times F_{ev,\alpha}$ and (**b**) $F_{ev,\beta} = 0.5 \times F_{ev,\alpha}$.

the size of the detector. Whatever the layer evaporation field or the set collection angle is, the main deviation is located at both interfaces and <10% (for a collection angle of 10°), whereas it is only a few percent for the rest (<3%). Despite this, as shown later, the effect of this remaining error is low on the overall reconstruction compared with a standard reconstruction.

Note that the analytical expression describing the evolution of the parameter μ_i [equation (12)] can be generalized to a microstructure composed of multiple stack layers (verified by simulation):

$$\mu_i = \left(\sum_{\varphi=\alpha}^{\omega} X_{\varphi,i} \left(\frac{F_{ev,\varphi}}{F_{ev,\alpha}} \right) \right)^{\frac{5}{3}} \times \left(\frac{V_i^*}{V_i} \right)^{\frac{2}{3}}, \tag{13}$$

with φ the different phases in the material (from α to ω), their associated evaporation field $F_{ev,\varphi}$, and $X_{\varphi,i}$ their concentration in the detector referential. The phase α is set as the reference phase.

Dynamic Reconstruction of Multilayered Structures

The application of the DR to a multilayered structure requires the definition and estimation of some parameters: the initial ICF (ξ_0) and field factor ($k_{f,0}$) (as used in the standard reconstruction), the different phases in order to estimate their concentration ($X_{\varphi,i}$), the reference potential (V_i^*), and the evaporation field ratio ($F_{ev,\varphi}/F_{ev,\alpha}$). With field evaporation simulation, those parameters are well known. Then, the relevance and validity of the DR can be tested since, in this case, the perfect reconstruction is known (as the original position of the atoms on the sample surface). From a visual inspection, it is obvious that the DR is closer to the perfect reconstruction than the standard and cone angle ones, whatever the values of the layer evaporation field (Figs. 3a, 3b). As nicely reproduced by the DR, the complex reconstructed morphology is due to the evolution of the magnification during evaporation (previously mentioned) and to the detector's finite size [more details can be found in Xu et al. (2015) and Rolland et al. (2017)].

Improvement in the comparison of the perfect and reconstructed spatial positions is also observed (Figs. 4a, 4b). As expected, the DR is not perfect but shows important signs of improvement compared with the standard and cone angle reconstructions. The main point is the limited error for the lateral reconstructed position (i.e., X), especially in the β layer in Figure 4. This partially contributes to limit the error shift in depth since the reconstruction protocol is an incremental process, based on the conservation of the volume. Deviations at the interface are also observed coming from (i) the relative error of the analytical approach for the evolution of μ [Fig. 2 and equation (12)] and (ii) the reconstruction protocol, assuming that the sample surface is hemispherical. Indeed, at the interfaces, the sample surface is not hemispherical and both phases (α and β) develop curvature. This is not considered in the DR (even in simulation results, Fig. 1), based on local averaging parameters. In response to this, other reconstruction parameters are added.

Experimentally, the dynamic parameters must be estimated since they are unknown. There exist different options to estimate the initial ICF (ξ_0) and field factor ($k_{f,0}$) (Gault et al., 2008, 2009; Loi et al., 2013) that the APT user can choose

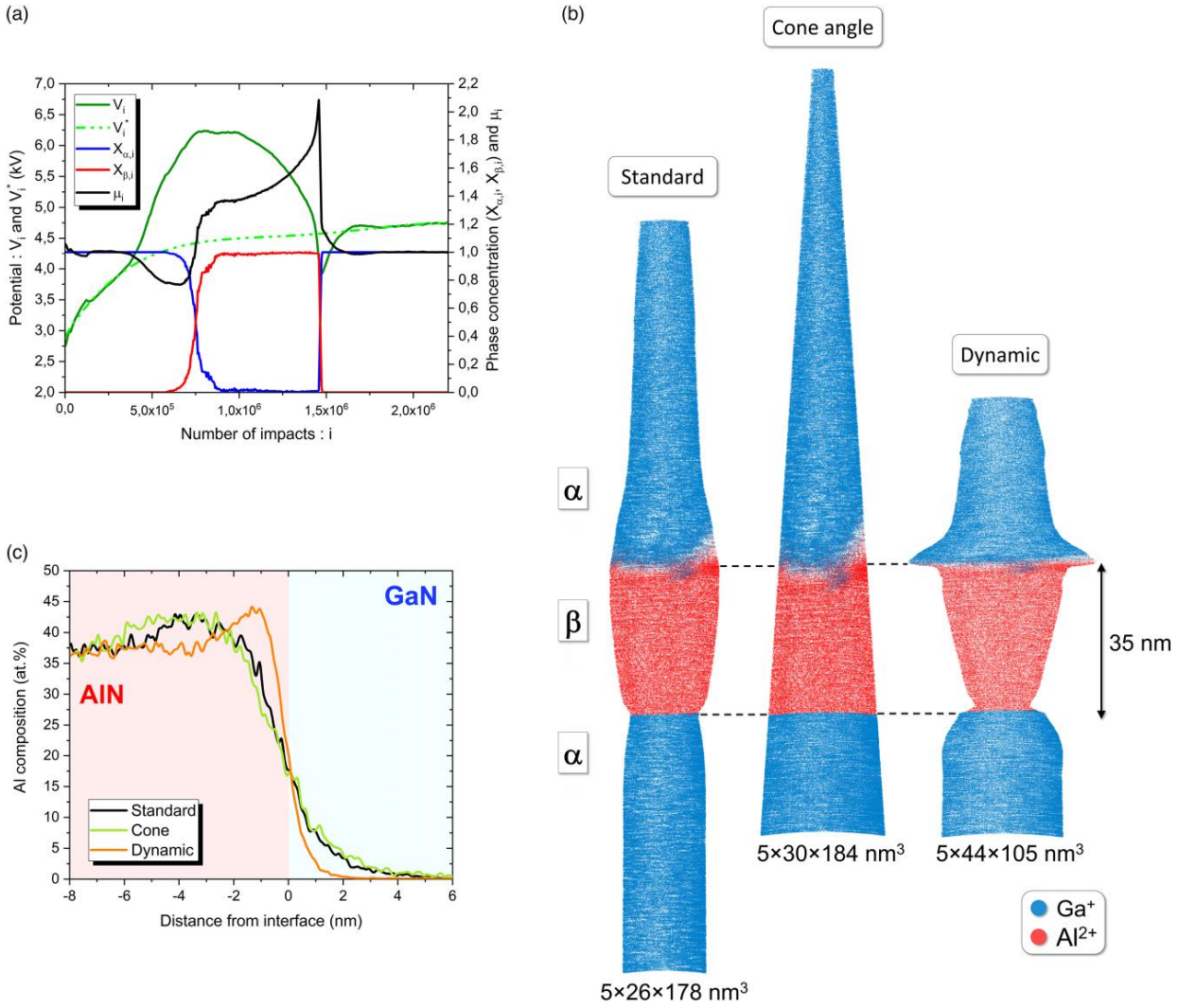

Fig. 5. (**a**) Applied potential (V_i) and reference potential (V_i^*) (in kV), phase concentrations $X_{\alpha,i}$ and $X_{\beta,i}$ corresponding, respectively, to phases rich in Ga^+ and Al^{2+}, and reconstruction parameter μ_i. (**b**) A 5 nm slice of the analyzed volume reconstruction, using different algorithms: standard, cone angle, and dynamic. (**c**) Proximity histogram (proxigram for short) Al concentration profile (steps of 0.1 nm) based on a 35 at% Ga iso-concentration surface (distance 0 represents the edge of the iso-surface).

from, adapted to their analyzed material. In the examples presented later, we will use *a priori* knowledge of the thickness of the layers. A binning of the atom sequence is performed to compute the evolution of the reconstruction parameters. This is essential to be able to estimate the different present phase concentrations. The number of atoms per bin must be chosen carefully. Indeed, a too-small number induces a lot of unreliable fluctuations and high measurement uncertainty, and a too-high number will smooth excessively, thus omitting important local evolutions of the reconstruction parameters, such as those at the interfaces. The concentration of each phase φ ($X_{\varphi,i}$) is estimated by choosing a chemical species that defines them. A fit of the potential curve associated with the reference phase (i.e., V_i for $X_{\alpha,i} = 1$ with a polynomial law) provides the reference potential (V_i^*). Based on field evaporation simulation results, the evaporation field ratio ($F_{ev,\varphi}/F_{ev,\alpha}$) can be estimated directly from the potential ratio V_i/V_i^* during the evaporation of the phase φ, if the relative thickness of the layer (e/R) is >50%. Otherwise, the layer thickness is too small to reach the equilibrium and thus a potential stabilization, corresponding then to the evaporation field ratio. In this case, the evaporation field ratio will be estimated with field evaporation simulation, adjusting the simulated evolution of the potential with the experimental one. Finally, the reconstruction parameters of each atom are calculated from linear interpolation according to its bin. The estimation of the reconstruction parameters and their evolution is performed for experimental data with a user interface NAPA developed in MATLAB® (Hatzoglou, 2022) and then used in the GPM 3D APT data treatment software.

Results

$In_{0.15}Al_{0.85}N/GaN$

The new algorithm was tested on an experimental dataset to investigate its applicability to real experiments. The sample is made up of an $In_{0.15}Al_{0.85}N$ layer of 35 nm embedded between two GaN layers. The initial ICF (ξ_0) and field factor ($k_{f,0}$) (and the initial radius R_0 for the cone angle reconstruction) are defined such that the reconstructed thickness of the

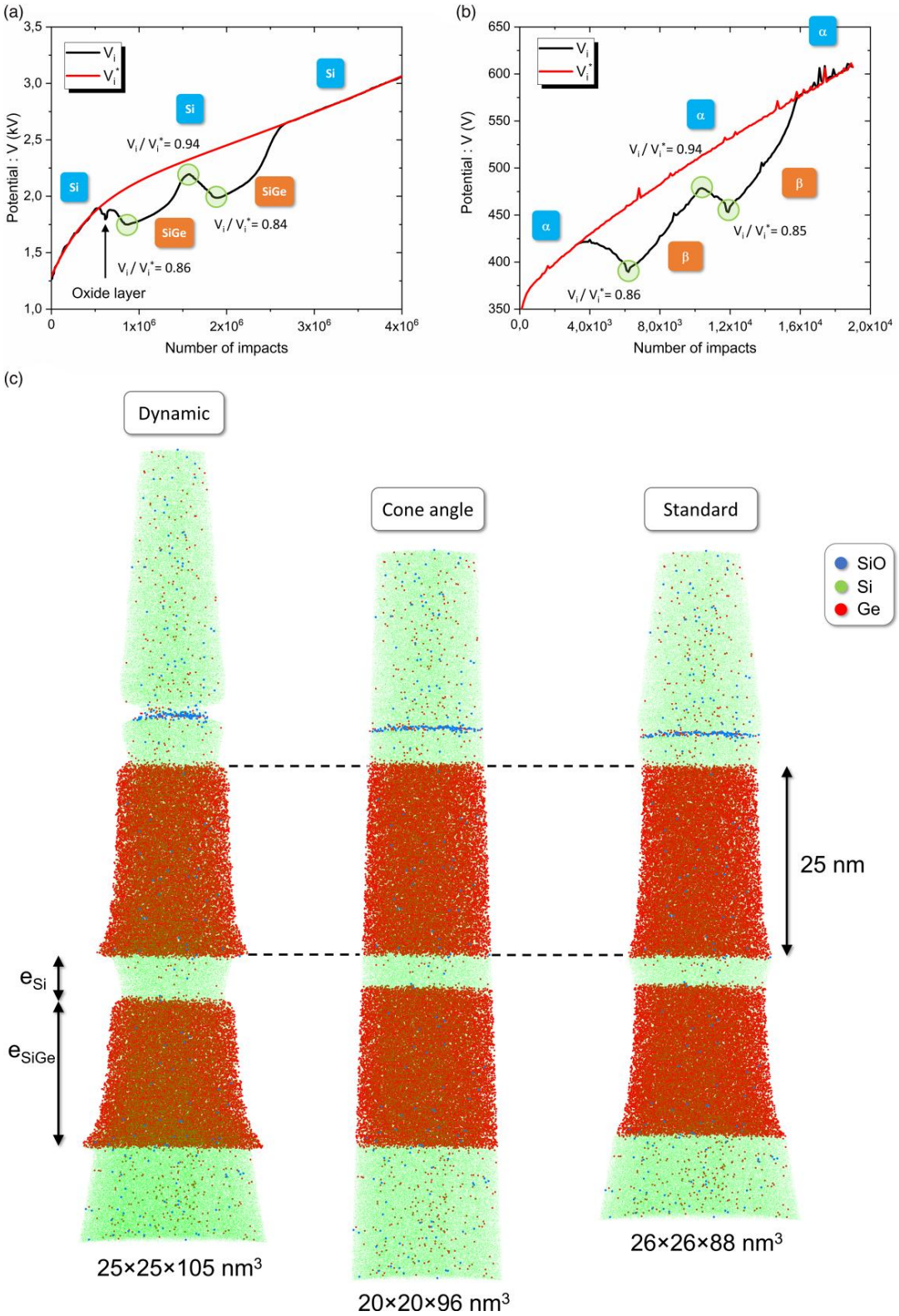

Fig. 6. (**a**) Experimental potential, (**b**) simulated applied potential (V_i), and reference potential (V_i^*). (**c**) Reconstruction of the analyzed volume, using different algorithms: dynamic, cone angle, and standard.

InAlN is equal to the expected one (i.e., 35 nm, Fig. 5a). As the first evaporated layer, the GaN layer is set as the reference layer for the DR (i.e., phase α) and is identified with Ga^{2+} ions. The InAlN layer (i.e., phase β) is identified with Al^{2+} ions (Fig. 5a). The reference potential (V_i^*) is obtained, adjusting the experimental potential (V_i) in the phase α ($X_{\alpha,i} = 1$) from two intervals: first to 0.3×10^6 impacts and 1.7×10^6 to the last impact. There is a stabilization of the potential

Table 1. Layer Thicknesses e_{Si} and e_{SiGe} (nm), Indexed in Figure 6c, as a Function of the Reconstruction (DR, Cone Angle, and Standard) and Compared with the Expected Values, Reported as Perfect.

Reconstruction	e_{Si} (nm)	e_{SiGe} (nm)
Perfect	10	21
Dynamic	7.6 ± 0.4	19.4 ± 0.4
Cone angle	5.0 ± 0.4	20.6 ± 0.4
Standard	4.4 ± 0.4	19.2 ± 0.4

These values were obtained from composition profiles along the evaporation direction.

(V_i^*) during the evaporation of the $In_{0.15}Al_{0.85}N$ layer (around 1×10^6 impacts), which was expected given the layer thickness (e) and the sample radius of curvature ($R_0 = 35$ nm, estimation from the cone angle reconstruction): $e/R_0 = 1$. In this condition, at this step of the evaporation, the evaporation field ratio $F_{ev,\beta}/F_{ev,\alpha}$ is thus equal to the potential ratio V_i/V_i^* and equal to 1.40 [close to the value obtained in Rolland et al. (2017) for the same material, i.e., 1.38].

The DR generally provides a reconstruction (Fig. 3a) with the expected layer thickness and flatter interfaces compared with the standard reconstructions (cone angle reconstruction or standard voltage-based reconstruction). We can also notice less diffuse (Fig. 5c) interfaces α/β with the DR. The standard and cone angle reconstructions do not consider the local increase in the radius of curvature at this interface (Fig. 1b), inducing then a contraction of the reconstruction lateral position and at the same time a bending of the interface (especially as the field of view is increasing). In contrast, the interface is flatter for the DR since the radius of curvature evolution is considered in this reconstruction protocol.

Si/SiGe

The next application is two layers of SiGe embedded in and separated by Si layers (Fig. 6c). In the evaporation direction, the two SiGe layer thicknesses are, respectively, equal to 25 and 21 nm (e_{SiGe} in Fig. 6c) and the distance between them is 10 nm (i.e., the Si layer thickness, indexed as e_{Si} in Fig. 6c). A silicon oxide layer is located upstream of the first SiGe layer. With this application, the applicability of the expression for multilayers is tested [equation (13)]. As done previously, the initial ICF (ξ_0) and field factor ($k_{f,0}$) (and the initial radius R_0 for the cone angle reconstruction) are defined such that the reconstructed thickness of the first layer of SiGe is equal to the expected one (i.e., 25 nm, Fig. 6c). The Si layers are set as the reference layer for the DR. However, the Si layer between the two SiGe layers is not considered to obtain the reference potential. In fact, the thickness of this layer is too small to reach the equilibrium ($e_{Si}/R_0 = 0.3$, Fig. 6a). This equilibrium is reached for the SiGe layers providing then their evaporation field ratio $F_{ev,SiGe}/F_{ev,Si}$, equal to 0.85 (using the ratio V_i/V_i^* during their evaporation). Also, due to its size (a few atomic layers), the silicon oxide layer does not reach equilibrium and the evaporation field ratio ($F_{ev,SiO}/F_{ev,Si}$) is set to 1.3 (more details in the next example). Those conclusions are verified with field evaporation simulation. Only SiGe layers in Si have been simulated, without a silicon oxide layer and with previously established parameters (i.e., layer thicknesses, radius of curvature, and evaporation field ratio). The results (Fig. 6b) coincide with the experimental results (Fig. 6a), thus validating the established reconstruction parameters.

Comparing the different reconstruction algorithms (Fig. 6c and Table 1), the Si layer thickness, between the two SiGe layers (e_{Si}), is clearly well underestimated by the standard and cone angle algorithms, whereas the DR provides a value closer to the expected one. The measurement of the SiGe layer (e_{SiGe}) is very similar for all the algorithms. Obviously, the DR produces a result closer to an ideal reconstruction and therefore produces more quantitative measurements in terms of dimensions.

Si/SiO$_2$

This application is a multilayered structure consisting of a successive stacking of Si (10 nm) and SiO_2 (4 nm) sublayers (Fig. 7), as observed by TEM (Li et al., 2017). As the feasibility and relevance of the DR have been already shown in the In0.15Al0.85N/GaN and Si/SiGe sections, this application will show the estimation of the evaporation field layer using simulation but also very clearly the morphological contribution of the DR.

There is no clear stabilization of the experimental potential (V_i) that could provide the evaporation field ratio ($F_{ev,SiO_2}/F_{ev,Si}$). This is expected considering the small layer thicknesses. Given these potential oscillations (Fig. 7a), it is difficult to understand the evaporation behavior and therefore to establish a reference potential (V_i^*). Using field evaporation simulation, these fluctuations appear to be induced by the SiO_2 layers having a high evaporation field (Fig. 7b), instead of a low field (Fig. 7c). This is even more evident by superimposing the evolution of the potential and the concentration of the phases in the reference frame of the detector. In addition, the simulation provides the trend of the reference potential; thus, values of the applied potential are used for fitting and then obtaining the experimental reference potential. The reference potential is obtained considering that the applied potential is equal to the reference one at the end of the evaporation of the SiO_2 layer (blue circles in Fig. 7a at the end of the potential decay) and then fitting these potential values with a polynomial law (V_i^* in Fig. 7a). The evaporation field ratio ($F_{ev,SiO_2}/F_{ev,Si}$) is then tuned in the simulation to obtain the experimental potential ratio (V_i/V_i^*). A good agreement is found for an evaporation field ratio equal to 1.3 (i.e., the ratio used in the previous application). As done up to now, the initial reconstruction parameters (for all algorithms) are set such that the SiO_2 layer thickness (the first one, id number 1) is equal to the expected one (i.e., 4 nm, Fig. 7d).

Clearly, DR provides a correct and constant SiO_2 layer thickness throughout the reconstruction (Fig. 7e) and, in addition, an overall morphology close to the expected one for this multilayered structure (Fig. 3). This is clearly not the case for the cone angle and standard reconstructions, which, respectively, under- and overestimated this layer thickness at the end of the reconstructed volume. For the Si layer thickness, all the algorithms overestimate it, with, however, a lower impact for the DR (≈7 nm, for the last layer), and the values are not constant throughout the reconstruction (Fig. 7e). If the dynamic initial parameters are defined using the first Si layer thickness (instead of SiO_2), the Si layer thickness still increases throughout the reconstruction, but the overestimation at the evaporation end is then very limited (1.6 nm, for the last layer). In return, the SiO_2 layer thickness is then underestimated (3 nm instead of 4 nm) but still constant. Correct thickness measurements for both layers (Si and SiO_2) are never

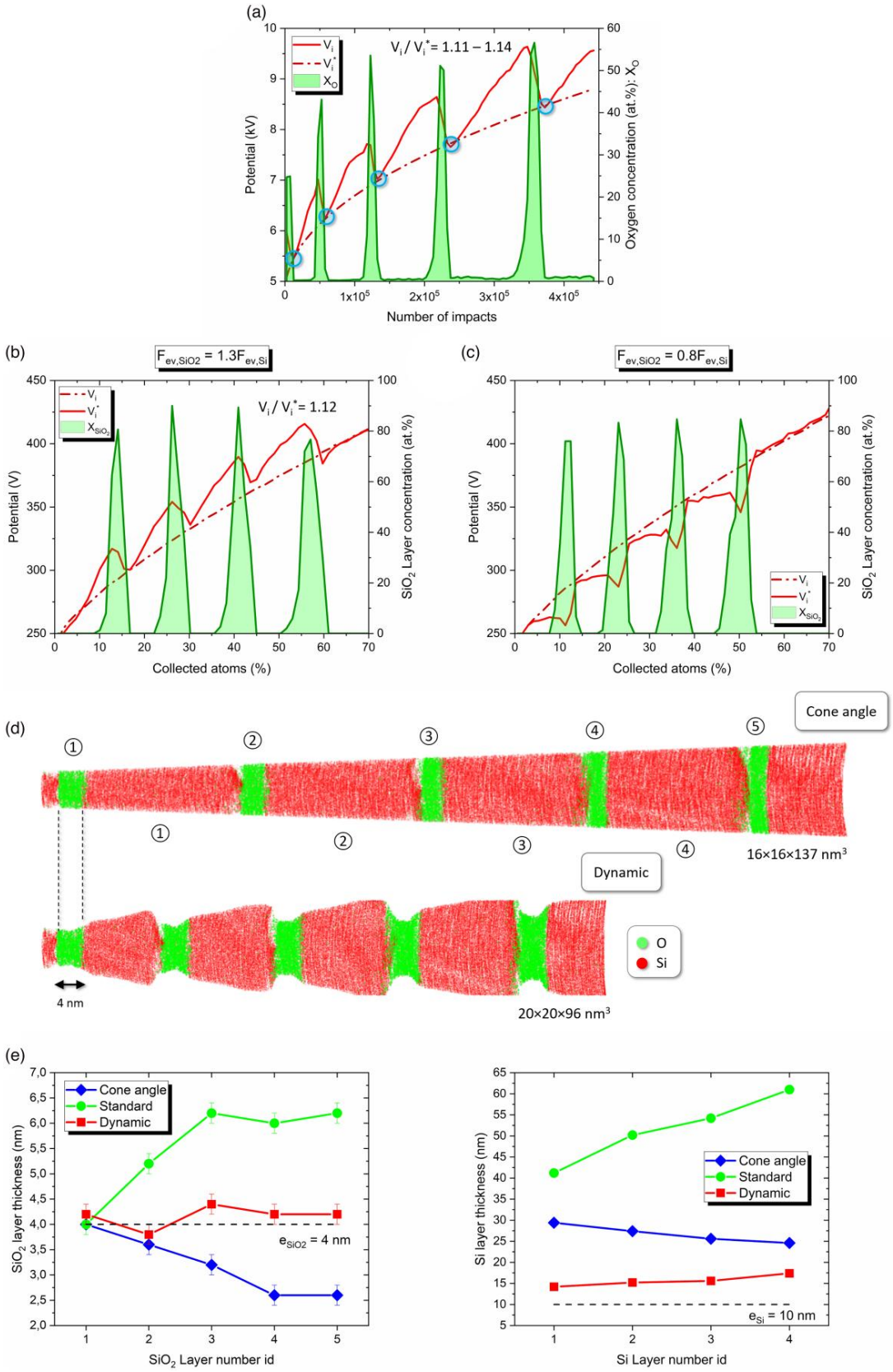

Fig. 7. (**a**) Experimental potential, simulated applied potential (V_i), and reference potential (V_i^*), according to the simulated evaporation field ratio $F_{ev,SiO_2}/F_{ev,Si}$: (**b**) 1.3 and (**c**) 0.8. (**d**) Reconstruction of the analyzed volume, using different algorithms: cone angle and dynamic. (**e**) SiO_2 and Si layer thickness measurements (nm), according to their id number (reported in Fig. 6d), for different reconstruction algorithms: cone angle, standard, and dynamic. The dashed lines correspond to the expected value for SiO_2 and Si layer thicknesses.

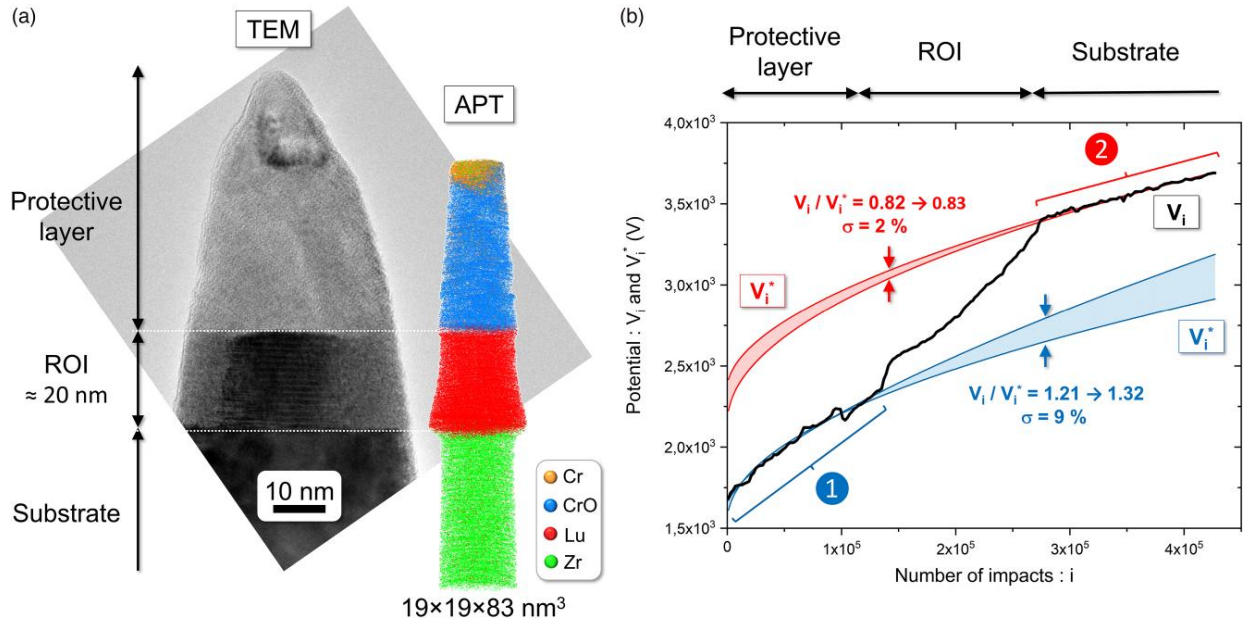

Fig. 8. (**a**) Transmission electron microscopy (TEM) of the sample before APT analysis and its reconstructed volume with DR. (**b**) Applied potential (V_i) and different estimations of the reference potential (V_i^*).

achieved at the same time along all the reconstructed volumes. The significant roughness of the interface (Fig. 7d) can explain some spread in the measurements but not its evolution throughout the reconstruction. A more likely hypothesis would be that one or both phases are subject to a nonquantification phenomenon (preferential evaporation, molecular dissociation, etc.), leading to incorrect mass identification. Indeed, in such cases, evaporated atoms are not quantified and thus do not contribute to the depth increment, inducing then, in the present studied case, an underestimation of thickness. A certain proportion of SiO molecular ions would be nonquantified, and the accurate stoichiometry being measured in the SiO_2 layer then induced the underestimation in layer thickness. This hypothesis seems reasonable since the concentration profiles do not show any atomic density fluctuations between the Si and SiO_2 layers, contrary to what is expected for such a structure. Indeed, the SiO_2 layers have an atomic density (66 at/nm^3) higher than that of the Si layers (50 at/nm^3) (Talbot et al., 2009). Thus, there is a lack of atom quantification for the SiO_2 layers (Zanuttini et al., 2017*a*, 2017*b*). The evolution of the thickness is unlikely to be directly due to the DR, since the latter is even capable of maintaining a constant atomic planar spacing of a single-phase material throughout the evaporation (Hatzoglou et al., 2019).

Clearly, the DR improves the reconstruction and therefore the accuracy of the measurements carried out. However, there remain some imperfections, which could be compensated by introducing a new dynamic parameter. Viewing the hypotheses considered above (nonquantification and mass spectra), detection efficiency could also be considered a dynamic parameter in future DR algorithm optimization (Diercks & Gorman, 2018).

LuFeO$_3$

The determination of the reference potential evolution (V_i^*) is an important point in DR. It is used for the evolution of the reconstruction parameters in equations (4) and (12) but also for the estimation of the phase evaporation field ratio (see the $In_{0.15}Al_{0.85}N$/GaN, Si/SiGe, and Si/SiO2 sections). In the previous examples, throughout the analysis, several significant points on the experimental potential curve (V_i) could be used to perform a fit to estimate the reference potential curve trend. Indeed, during the analysis, we intercepted several times the phase chosen as the reference.

The reference potential curve estimation will be discussed in this last application. It is a layer of $LuFeO_3$ thin film grown on a substrate of YSZ (yttrium-stabilized zirconia) with a protective layer above (CrO) (Moyer et al., 2014; Disseler et al., 2015). The TEM observations, on the sample before APT analysis (Fig. 8a), show a $LuFeO_3$ film thickness of ~20 nm (used to calibrate dynamic parameters). As in the previous examples, if the first evaporated layer is chosen as the reference, then, in the present case, the number of points on the experimental potential curve (Fig. 8b) that can be used to estimate the evolution of the reference potential is limited at the beginning of the analysis (annotated as 1 in Fig. 8b). There are therefore no other points of interest at the end or in the process of analysis to which we could relate to estimate the relevance of the fit. In addition, some fluctuations should not be considered, which further reduces the number of points for fitting. Finally, the type of equation retained for the fit plays a major role, without having absolute certainty about its validity. Figure 7b shows the spread of the estimated reference potential curve considering the points previously mentioned (selected data, fluctuations, and type of equation). Consequently, the phase evaporation field ratio estimation can be significantly modified, biasing the reconstruction. Indeed, the evaporation field ratio between the substrate and the protective layer varies from 1.2 to 1.3 according to the selected data for the fit and the equation type (Fig. 8b). We can therefore see here that according to the estimation procedure chosen by the user, this will influence the DR. From field evaporation simulation, it could be considered to tabulate the

evolution of the potential curve according to the shank angle and the radius of curvature of the sample. This also leads to adding more reconstruction parameters in a procedure that already contains many.

In the present case, in order to be able to carry out a DR, we have chosen to estimate the evolution of the potential curve from the last evaporated phase (i.e., the substrate, annotated as 2 in Fig. 8b). The potential trend is almost linear without fluctuations. We are still confronted with the choice of the fit equation. However, with the last layer selection approach, the error made will be mainly focused on the beginning of the analysis (i.e., the protective layer), with the same type of equation previously used. For this material in particular, the region of interest is the $LuFeO_3$ layer and its interface with the substrate. We therefore limit the error in a dedicated studied region but potentially increase the error further away from the region of interest. A 2 nm variation of the measured thickness in the layer (i.e., 10% of the expected thickness) can be observed depending on the region and the type of fit used. Despite these potential errors, the DR is still able to correctly reproduce the complex reconstructed morphology due to the evolution of the magnification during evaporation (Fig. 8a). In this example, the layers are thick enough to reach equilibrium during their evaporation and therefore a stabilization of the potential. It is thus possible to use the last evaporated layer to estimate the reference potential. However, in the case where the layers are very thin ($e/R_0 < 0.5$), the estimation of the potential (and therefore the relevance to the reconstruction) from the first phase depends on the user's choices.

Conclusion

By expanding previous approaches for homogeneous materials (Hatzoglou et al., 2019), it was possible to estimate the evolution of the reconstruction parameters throughout the APT sample evaporation for multilayered structures using field evaporation simulation. Implementation of the evolution of these factors in the reconstruction protocol, named DR, produces a significant improvement in the reconstruction accuracy. In return, a new parameter is added (i.e., μ_i). We have shown how it is possible to estimate it (from raw experimental data or using field evaporation simulation), but *a priori* knowledge of the analyzed structure (e.g., the layer thickness) is necessary to perform an accurate calibration. This is already the case for current reconstruction methods. In all the cases presented here, the application of DR to experimental analyses exhibits an improvement in the 3D reconstruction (in terms of reconstructed shape, interface, sharpness, and spatial measurements) in comparison with current reconstruction methods. In all the examples and simulations presented in this study, the interfaces are perpendicular to the analysis direction. One possibility to expand the DR toward tilted (multi)layered structures (Perrin Toinin et al., 2023) is to involve the lateral evolution of the reconstruction parameters based on the radial position of impacts on the detector. The results here represent an important step toward a more accurate APT analysis of multilayered systems, which is important to understand their complex physics and emergent interface phenomena.

Acknowledgments

The authors are grateful for scientific and technical input and support from Semiconductor Research Corporation (SRC) under task ID 2679.001. The Research Council of Norway (RCN) is acknowledged for its support to the Norwegian Micro- and Nano-Fabrication Facility, NorFab, project number 295864; the Norwegian Laboratory for Mineral and Materials Characterization, MiMaC, project number 269842/F50; and the Norwegian Center for Transmission Electron Microscopy, NORTEM (197405/F50). K.A.H. and D.M. thank the Department of Materials Science and Engineering at NTNU for direct financial support. D.M. acknowledges funding from the European Research Council (ERC) under the European Union's Horizon 2020 research and innovation program (Grant Agreement No. 863691). D.M. thanks NTNU for support through the Onsager Fellowship Program and NTNU Stjerneprogrammet. The authors thank C.M. Brooks, M. Holtz, D.G. Schlom, and J.A. Mundy for providing the $LuFeO_3$ thin film for this study.

Financial Support

The current study hasn't received any fund from any organizations or institutions.

Conflict of Interest

The authors declare that they have no competing interest.

References

Bas P, Bostel A, Deconihout B & Blavette D (1995). A general protocol for the reconstruction of 3D atom probe data. *Appl Surf Sci* **87-88**, 298–304. https://doi.org/10.1016/0169-4332(94)00561-3

Beinke D, Oberdorfer C & Schmitz G (2016). Towards an accurate volume reconstruction in atom probe tomography. *Ultramicroscopy* **165**, 34–41. https://doi.org/10.1016/j.ultramic.2016.03.008

Diercks DR & Gorman BP (2018). Self-consistent atom probe tomography reconstructions utilizing electron microscopy. *Ultramicroscopy* **195**, 32–46. https://doi.org/10.1016/j.ultramic.2018.08.019

Disseler SM, Borchers JA, Brooks CM, Mundy JA, Moyer JA, Hillsberry DA, Thies EL, Tenne DA, Heron J, Holtz ME, Clarkson JD, Stiehl GM, Schiffer P, Muller DA, Schlom DG & Ratcliff WD (2015). Magnetic structure and ordering of multiferroic hexagonal $LuFeO_3$. *Phys Rev Lett* **114**, 217602. https://doi.org/10.1103/PhysRevLett.114.217602

Fletcher C, Moody MP, Fleischmann C, Dialameh M, Porret C, Geiser B & Haley D (2022). Automated calibration of model-driven reconstructions in atom probe tomography. *J Phys D* **55**, 375301. https://doi.org/10.1088/1361-6463/ac7986

Gault B, de Geuser F, Stephenson LT, Moody MP, Muddle BC & Ringer SP (2008). Estimation of the reconstruction parameters for atom probe tomography. *Microsc Microanal* **14**, 296–305. https://doi.org/10.1017/S1431927608080690

Gault B, Haley D, de Geuser F, Moody MP, Marquis EA, Larson DJ & Geiser BP (2011a). Advances in the reconstruction of atom probe tomography data. *Ultramicroscopy* **111**, 448–457. https://doi.org/10.1016/j.ultramic.2010.11.016

Gault B, Loi ST, Araullo-Peters VJ, Stephenson LT, Moody MP, Shrestha SL, Marceau RKW, Yao L, Cairney JM & Ringer SP (2011b). Dynamic reconstruction for atom probe tomography. *Ultramicroscopy* **111**, 1619–1624. https://doi.org/10.1016/j.ultramic.2011.08.005

Gault B, Moody MP, Cairney JM & Ringer SP (2012). *Atom Probe Microscopy*. Berlin: Springer Science & Business Media.

Gault B, Moody MP, de Geuser F, Tsafnat G, La Fontaine A, Stephenson LT, Haley D & Ringer SP (2009). Advances in the

calibration of atom probe tomographic reconstruction. *J Appl Phys* **105**, 034913. https://doi.org/10.1063/1.3068197

Geiser BP, Larson DJ, Oltman E, Gerstl S, Reinhard D, Kelly TF & Prosa TJ (2009). Wide-field-of-view atom probe reconstruction. *Microsc Microanal* **15**, 292–293. https://doi.org/10.1017/S1431927609098249

Haley D, Bagot PAJ & Moody MP (2018). Extending continuum models for atom probe simulation. *Mater Charact* **146**, 299–306. https://doi.org/10.1016/j.matchar.2018.02.032

Haley D, Moody MP & Smith GDW (2013). Level set methods for modelling field evaporation in atom probe. *Microsc Microanal* **19**, 1709–1717. https://doi.org/10.1017/S1431927613013299

Haley D, Petersen T, Ringer SP & Smith GDW (2011). Atom probe trajectory mapping using experimental tip shape measurements. *J Microscopy* **244**, 170–180. https://doi.org/10.1111/j.1365-2818.2011.03522.x

Hatzoglou, C. (2022). *Norwegian University of Science and Technology —Atom Probe Tomography Lab*. https://www.ntnu.edu/ima/research/apt

Hatzoglou C, Da Costa G & Vurpillot F (2019). Enhanced dynamic reconstruction for atom probe tomography. *Ultramicroscopy* **197**, 72–82. https://doi.org/10.1016/j.ultramic.2018.11.010

Herbig M, Choi P & Raabe D (2015). Combining structural and chemical information at the nanometer scale by correlative transmission electron microscopy and atom probe tomography. *Ultramicroscopy* **153**, 32–39. https://doi.org/10.1016/j.ultramic.2015.02.003

Jeske T & Schmitz G (2001). Nanoscale analysis of the early interreaction stages in Al/Ni. *Scr Mater* **45**, 555–560. https://doi.org/10.1016/S1359-6462(01)01058-2

Larson DJ, Geiser BP, Prosa TJ, Gerstl SSA, Reinhard DA & Kelly TF (2011). Improvements in planar feature reconstructions in atom probe tomography. *J Microscopy* **243**, 15–30. https://doi.org/10.1111/j.1365-2818.2010.03474.x

Larson DJ, Geiser BP, Prosa TJ & Kelly TF (2012). On the use of simulated field-evaporated specimen apex shapes in atom probe tomography data reconstruction. *Microsc Microanal* **18**, 953–963. https://doi.org/10.1017/S1431927612001523

Larson DJ, Prosa TJ, Ulfig RM, Geiser BP & Kelly TF (2013). *Local Electrode Atom Probe Tomography: A User's Guide*. New York: Springer-Verlag. (Accessed April 24, 2020).

Lefebvre W, Vurpillot F & Sauvage X (2016). *Atom Probe Tomography: Put Theory into Practice*. Boston, MA: Elsevier.

Li D, Jiang Y, Zhang P, Shan D, Xu J, Li W & Chen K (2017). The phosphorus and boron co-doping behaviors at nanoscale in Si nanocrystals/SiO_2 multilayers. *Appl Phys Lett* **110**, 233105. https://doi.org/10.1063/1.4984949

Loi ST, Gault B, Ringer SP, Larson DJ & Geiser BP (2013). Electrostatic simulations of a local electrode atom probe: The dependence of tomographic reconstruction parameters on specimen and microscope geometry. *Ultramicroscopy* **132**, 107–113. https://doi.org/10.1016/j.ultramic.2012.12.012

Marquis EA, Geiser BP, Prosa TJ & Larson DJ (2011). Evolution of tip shape during field evaporation of complex multilayer structures. *J Microscopy* **241**, 225–233. https://doi.org/10.1111/j.1365-2818.2010.03421.x

Mesa G, Dobado-Fuentes E & Sáenz JJ (1996). Image charge method for electrostatic calculations in field-emission diodes. *J Appl Phys* **79**, 39–44. https://doi.org/10.1063/1.360951

Miller, M. K. (2000). *Atom Probe Tomography: Analysis at the Atomic Level*. New York: Springer.

Miller MK & Forbes RG (2009). Atom probe tomography. *Mater Charact* **60**, 461–469. https://doi.org/10.1016/j.matchar.2009.02.007

Moyer JA, Misra R, Mundy JA, Brooks CM, Heron JT, Muller DA, Schlom DG & Schiffer P (2014). Intrinsic magnetic properties of hexagonal $LuFeO_3$ and the effects of nonstoichiometry. *APL Mater* **2**, 012106. https://doi.org/10.1063/1.4861795

Perrin Toinin J, Hatzoglou C, Voronkoff J, Montigaud H, Guimard D, Wuttig M, Vurpillot F & Cojocaru-Mirédin O (2023). A quantitative investigation of functionalized glazing stacks by atom probe tomography. *Adv Mater Technol* **8**, 2200922. https://doi.org/10.1002/admt.202200922

Rolland N, Larson DJ, Geiser BP, Duguay S, Vurpillot F & Blavette D (2015a). An analytical model accounting for tip shape evolution during atom probe analysis of heterogeneous materials. *Ultramicroscopy* **159**, 195–201. https://doi.org/10.1016/j.ultramic.2015.03.010

Rolland N, Vurpillot F, Duguay S & Blavette D (2015b). Dynamic evolution and fracture of multilayer field emitters in atom probe tomography: A new interpretation. *Eur Phys J Appl Phys* **72**, 21001. https://doi.org/10.1051/epjap/2015150233

Rolland N, Vurpillot F, Duguay S, Mazumder B, Speck JS & Blavette D (2017). New atom probe tomography reconstruction algorithm for multilayered samples: Beyond the hemispherical constraint. *Microsc Microanal* **23**, 247–254. https://doi.org/10.1017/S1431927617000253

Talbot E, Larde R, Gourbilleau F, Dufour C & Pareige P (2009). Si nanoparticles in SiO_2: An atomic scale observation for optimization of optical devices. *EPL* **87**, 26004. https://doi.org/10.1209/0295-5075/87/26004

Vurpillot F, Bostel A, Menand A & Blavette D (1999). Trajectories of field emitted ions in 3D atom-probe. *Eur Phys J* **6**, 217–221. https://doi.org/10.1051/epjap:1999173

Vurpillot F, Gaillard A, Da Costa G & Deconihout B (2013a). A model to predict image formation in atom probe tomography. *Ultramicroscopy* **132**, 152–157. https://doi.org/10.1016/j.ultramic.2012.12.007

Vurpillot F, Gault B, Geiser BP & Larson DJ (2013b). Reconstructing atom probe data: A review. *Ultramicroscopy* **132**, 19–30. https://doi.org/10.1016/j.ultramic.2013.03.010

Vurpillot F, Gruber M, Da Costa G, Martin I, Renaud L & Bostel A (2011). Pragmatic reconstruction methods in atom probe tomography. *Ultramicroscopy* **111**, 1286–1294. https://doi.org/10.1016/j.ultramic.2011.04.001

Vurpillot F, Larson DJ & Cerezo A (2004). Improvement of multilayer analyses with a three-dimensional atom probe. *Surf Interface Anal* **36**, 552–558. https://doi.org/10.1002/sia.1697

Vurpillot F & Oberdorfer C (2015). Modeling atom probe tomography: A review. *Ultramicroscopy* **159**, 202–216. https://doi.org/10.1016/j.ultramic.2014.12.013

Vurpillot F, Rolland N, Estivill R, Duguay S & Blavette D (2016). Accuracy of analyses of microelectronics nanostructures in atom probe tomography. *Semicond Sci Technol* **31**, 074002. https://doi.org/10.1088/0268-1242/31/7/074002

Walck SD, Buyuklimanli T & Hren JJ (1986). Extended depth profiling with the IAP. *J. Phys* **47-C2**(3), 451–458.

Xu Z, Li D, Xu W, Devaraj A, Colby R, Thevuthasan S, Geiser BP & Larson DJ (2015). Simulation of heterogeneous atom probe tip shapes evolution during field evaporation using a level set method and different evaporation models. *Comput Phys Commun* **189**, 106–113. https://doi.org/10.1016/j.cpc.2014.12.016

Zanuttini D, Blum I, Rigutti L, Vurpillot F, Douady J, Jacquet E, Anglade P-M & Gervais B (2017a). Electronic structure and stability of the SiO_2+ dications produced in tomographic atom probe experiments. *J Chem Phys* **147**, 164301. https://doi.org/10.1063/1.5001113

Zanuttini D, Blum I, Rigutti L, Vurpillot F, Douady J, Jacquet E, Anglade P-M & Gervais B (2017b). Simulation of field-induced molecular dissociation in atom-probe tomography: Identification of a neutral emission channel. *Phys Rev A* **95**, 061401. https://doi.org/10.1103/PhysRevA.95.061401